AIAA JOURNAL
Vol. 46, No. 1, January 2008

Comparison of High-Altitude Hypersonic Wake Flows of Slender and Blunt Bodies

Jiaqiang Zhong,* Takashi Ozawa,† and Deborah A. Levin‡
Pennsylvania State University, University Park, Pennsylvania 16802

DOI: 10.2514/1.31056

The gas dynamic features of the laminar, near-wake flow behind slender and blunt hypersonic vehicles are studied using the direct simulation Monte Carlo method. Near-wake flows are characterized by features of low density, low Reynolds number, high temperature, thermal nonequilibrium, species separation, and recirculation. The impact of freestream number density and velocity on the near-wake flowfield is considered and compared for slender and blunt bodies. The near-wake structure postulated by theory and observed in numerical continuum calculations is also observed in the kinetic simulations, which are more accurate in the high-altitude, rarefied near-wake flow. The paper discusses the validation of the direct simulation Monte Carlo computational tool with experimental data for slender and blunt shapes and a previously published blunt direct simulation Monte Carlo geometry case. Then, the near-wake flows generated by a 10 deg slender cone and a 70 deg blunt body are analyzed. The near-wake flows behind slender and blunt bodies are similar in that the freestream Mach number has little impact on the near-wake flow structure and the recirculation length is not found to be related to the local Reynolds number. For both geometries, the base radius was found to be the characteristic length in the near-wake flow. Significant differences in the near-wake flow for the two geometries were observed in the spatial distribution of gas temperatures, the degree of chemical dissociation, and the sensitivity of recirculation length to freestream number density.

Nomenclature

b	=	axial distance to base surface normalized to base radius
D	=	base diameter
L	=	body length
N_d	=	number density
P	=	pressure
R	=	base radius
Rd	=	dissociation rate
Re	=	Reynolds number
T	=	temperature
U	=	axial velocity
Y	=	radial position
ρ	=	density

Subscripts

s	=	stagnation state
∞	=	freestream condition

I. Introduction

THE wake flowfield of a hypersonic vehicle has recently become of great interest [1–4] because it influences vehicle stability, base heating, and optical emissions from nonthrusting vehicles. Although the base pressure contributes a small proportion to the total drag, the control of flight vehicle trajectory and posture requires accurate base pressure estimation [5]. The intense aerodynamic heating that hypersonic vehicles are subjected to requires the accurate design of thermal protection systems to prevent damage to the vehicle at a minimal weight penalty [6]. Optical emissions from wake flows are potentially important for the detection, tracking, and discrimination of target vehicles [7,8].

However, the modeling and simulation of reentry flows is quite challenging due to the complexities of including realistic gas chemical reactions, ionization for high Mach number reentries [9], gas-surface reactions, surface sublimation [10], and mechanical ablation [11], to name a few. Moreover, the lack of theoretical analysis and experimental data of hypersonic vehicle near-wake flows at high altitudes makes computational investigation crucial to future planetary and solar system exploration [12] as well as military space missions. Ground testing is important for validation of flow features that may be scaled by size and freestream characteristics and are not too strongly affected by rarefaction effects. A recent review of published afterbody aeroheating flight data in the continuum flight regime may be found in the work of Wright et al. [13]. However, in-flight testing is crucial for understanding all of the operational aspects that may not be predicted by idealized modeling and simulation, but the cost of adequately instrumented flight tests remains an important concern. For this reason, planning for future flight-test programs should emphasize, wherever possible, commonality of U.S. Department of Defense (DoD) and NASA high-altitude flow phenomena. To that end, the main objective of this work is to study and compare the near-wake flowfields of slender and blunt bodies at high altitudes by taking into account rarefaction affects.

The gas dynamic features of the near wake have been discussed by a number of authors. In the near-wake region [14], viscous forces dominate over inertial ones such that the gas flow moving downstream tends to be stopped and turned back upstream, forming a nonequilibrium recirculation region of high temperatures. Figure 1 shows the typical schematics of the near-wake flow structure [15] for slender and blunt bodies. A detached bow shock for the blunt body or attached oblique shock for the slender body (a) is developed in a thin region leading to a sudden increase of pressure, temperature, and density. A boundary layer is developed in a region close to the body surface, and the gas at the shoulder undergoes a rapid expansion (e), starting from the leading-edge wave and ending at a trailing-edge wave. Under the influence of viscous and pressure forces, the boundary layer separates from the body to form a free shear layer (s). The expansion waves are compressed (c) after they reach the outer shock flow and inner viscous wake. The dividing streamline (d),

Presented as Paper 612 at the 45th AIAA Aerospace Science Meeting, Reno, NV, 8–11 January 2007; received 15 March 2007; revision received 10 October 2007; accepted for publication 10 October 2007.

*Postdoctoral Research Fellow, Department of Aerospace Engineering. AIAA Member.

†Graduate Student, Department of Aerospace Engineering. AIAA Student Member.

‡Associate Professor, Department of Aerospace Engineering. AIAA Associate Fellow.

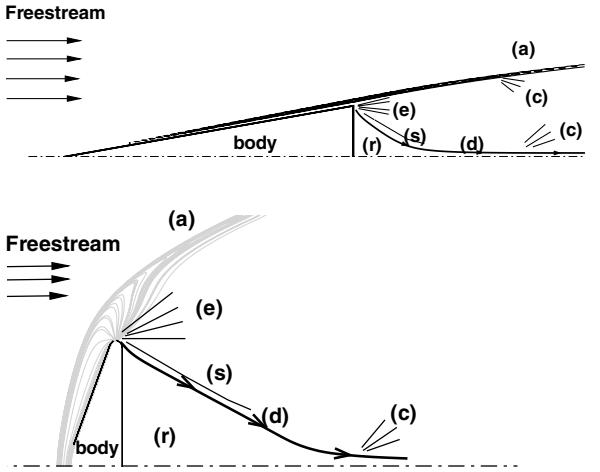

Fig. 1 Schematic of near-wake flows for slender (top) and blunt bodies (bottom) : bow shock (a), expanding flow (e), shear layer (s), compression shock (c), recirculation region (r), and dividing streamline (d). Contours represent gas number density.

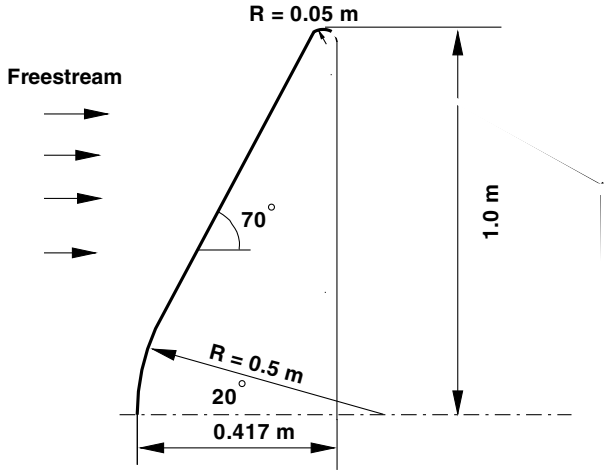

Fig. 2 Blunt body geometry configuration [3].

which originates at the shoulder position, separates the recirculation region (r) from the flow that continues downstream. Because the detached bow shock of the blunt body is much stronger than the attached shock of the slender body, the gas species mole fraction may be significantly different in the near-wake region for the slender and blunt bodies due to a higher chemical reaction rate in the blunt body bow-shock region.

Hypersonic wake flows have been numerically modeled by a number of researchers and here we only mention a few papers that are primarily concerned with the modeling of near-wake laminar recirculation flows. Grasso and Pettinelli [1] investigated the influence of geometry and Mach and Reynolds numbers on the hypersonic near-wake structure by solving the full compressible Navier–Stokes equations. The test cases discussed in their work were for Reynolds numbers of $\sim 10^3$–10^6 and Mach numbers of ~ 10 corresponding to a Knudsen range of $\sim 10^{-2}$–10^{-5}. They further studied real gas thermal and chemical nonequilibrium effects in near-wake flows accounting for dissociation and ionization processes [2]. Dogra et al. [3] applied the kinetic, direct simulation Monte Carlo (DSMC) and continuum Navier–Stokes methods to study a 70 deg blunt body with a freestream velocity of 7 km/s at an altitude of 85 km, showing that species separation for heavy and light particles occurs in the near-wake region. Recently, Lin et al. [4] used a Reynolds-averaged Navier–Stokes code to investigate hypersonic reentry vehicle near-wake flow structures, base pressure, and heating distributions at various angles of attack at an altitude of 38 km.

As will be shown in this work, the near-wake reentry flow above 80 km is characterized by nonequilibrium, and the continuum approach is not strictly applicable due to the rarefied effects. The accurate modeling of such flows requires a particle-based kinetic simulation method. An objective of this work is to apply the direct simulation Monte Carlo [16,17] approach to study the low Reynolds number, nonequilibrium, and recirculation flows in the near-wake region. In this work, we study the near-wake flows behind a 10 deg half-angle cone slender body at an altitude of 80 km, and a 70 deg blunt body at an altitude of 85 km. The blunt body, as shown in Fig. 2, is chosen from a space vehicle configuration proposed for Mars environmental survey [3]. The slender body geometry is motivated by the test shape used in the wind-tunnel tests of Holden [18]. The remainder of the paper is organized as follows. The DSMC near-wake flow results are validated in Sec. II by comparing simulation results with experimental temperature, velocity, and pressure data for slender cones and a cylindrical shape, along the axial and radial directions, respectively. In Sec. III, we discuss in detail the near-wake flow characteristics for both slender and blunt bodies, and analyze the parameters that strongly affect the recirculation structure. Conclusions are summarized in Sec. IV for both slender and blunt bodies and the recirculation structure.

II. Validation Cases

In this section, we consider four validation cases for our DSMC calculations. The first two are experimental studies of near-body slender wake flows [19,20], the third is an experimental study of a blunt cylinder near-body wake flow [21], and the last one is a computation of a blunt space vehicle entry wake flow [3]. To the best of our knowledge [22], this work presents the first comparison of these experimental data with numerical DSMC simulations.

Todisco and Pallone [19] measured the near-wake laminar flow of a 10 deg half-angle cone with a base diameter of 3.26 in. at zero angle of attack. The test was performed in a 20 in. hypersonic shock tunnel, using a 1.5 in. straight double diaphragm shock tube to measure gas stagnation enthalpy, and a constant hot-wire technique to measure gas temperature. The test gas was air, with a freestream Mach number of 16.0, a temperature of 54 K, and pressures of 4.3 and 36.5 Pa.

For the simulations presented in this work, the two-dimensional axisymmetric DSMC-based statistical method in low density environment (SMILE) code [17] is used. The majorant frequency scheme is used to calculate collision pairs, the variable hard sphere model is used as the molecular collision model, and the Larsen–Borgnakke model is used for energy exchange between the translational and internal modes.

The DSMC numerical solution depends on three parameters, the cell size Δx, time step Δt, and the number of simulated particles. In the DSMC algorithm, the cell size is on the same order of the local mean free path, and the duration of each time step is on the order of mean collision time. The number of simulated particles needs to be large enough to ensure that correlations between particles are insignificant and statistical errors are small. To establish grid and particle convergence and assess the numerical accuracy of the calculations, we performed a numerical study of the low-pressure Todisco and Pallone [19] case. The computational domain extends 80×480 mm in the radial and flow directions. It was observed from the simulation results that the axial velocity distribution along the wake flow centerline does not change as the time step is decreased from 2×10^{-7} to 5×10^{-8} s. In the three numerical test simulations, we choose one simulated particle to represent $2.5 \times 10^{+11}$, $1.0 \times 10^{+11}$, and $5.0 \times 10^{+10}$ real particles to test the impact of number of simulated particles on the numerical results. For these three cases, there are about $1.68 \times 10^{+6}$, $4.25 \times 10^{+6}$, and $8.48 \times 10^{+6}$ simulated particles in the computational domain. It was found that the axial flow velocity along the wake centerline is converged with respect to the number of simulated particles. Because the local mean free path may vary significantly through the computational domain, the collision cell adaption is used to automatically divide an original cell into smaller cells based on the local flow gradient. Figure 3 shows pressure distribution along the wake flow centerline for simulations performed with 15,000, 60,000, and 93,750 cells in the computational domain, corresponding to a cell size of 1.6×10^{-3}, 8.0×10^{-4}, and 6.4×10^{-4} m. The influence of the number of cells,

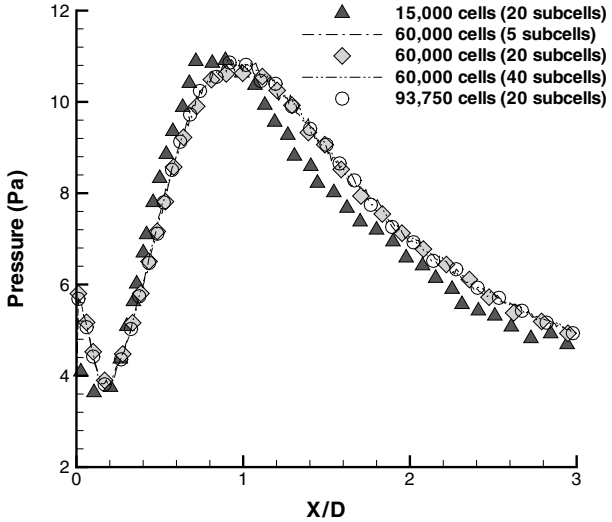

Fig. 3 Pressure distribution along the wake flow centerline for different numbers of cells.

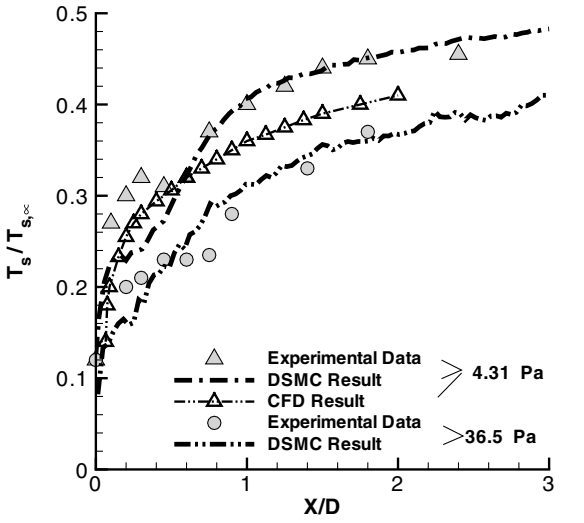

Fig. 4 Comparison of the ratio of stagnation temperature to the total temperature along the wake centerline between the experimental data (solid symbols) [19] and simulation results (lines). CFD results (open symbols) are those of Grasso and Pettinelli [1].

as well as the degree of adaption on the pressure profile was not observed because the cell size is less than 8.0×10^{-3} m. An average percent difference in the pressure distribution given in Fig. 3 between the simulations obtained with 60,000 vs 15,000 cells is less than 5%. Note that the number of subcells could be important in a high gradient shock region. In summary, we choose 60,000 cells, 4.25 million simulated particles, and a time step of 1.0×10^{-7} s for all calculations presented hereafter.

Figure 4 compares the DSMC simulation results (lines) of nondimensional temperature, the ratio of stagnation temperature to the total temperature, along the wake centerline with the experimental data (solid symbols), as shown in Fig. 11 in Todisco and Pallone's paper [19]. Our simulation results agree with experimental data reasonably well at a location of about 0.6 times the base diameter downstream from the base, whereas upstream at the location close to the base there is approximately a 30% difference between the simulation results and experimental data. Grasso and Pettinelli also validated the near-wake temperatures for the freestream pressure 4.3 Pa case by solving the full laminar compressible Navier–Stokes equations, as shown in Fig. 5 of their paper. [1] It can be seen in Fig. 4 that their continuum CFD solution is generally lower than the DSMC solution and experimental data. Because the near-wake flow for this case has a local Knudsen number

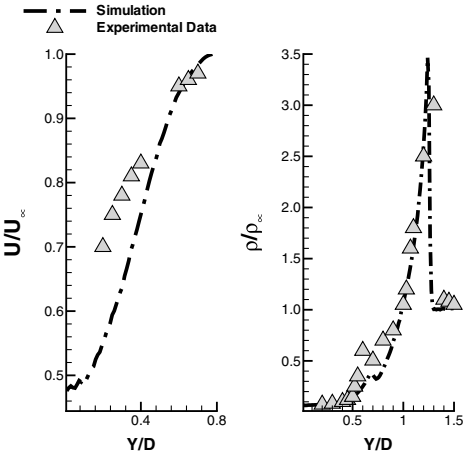

Fig. 5 Comparison of the ratio of wake flow *U* velocity (left) and density to the freestream values along the radial direction at a location three times the base diameter distance downstream of the cone base between the experimental data (symbols) [20] and DSMC simulation results (lines).

of about $0.01 \sim 0.08$, based on the base radius, the rarefied feature of the flow suggests that the DSMC results will be more accurate than a continuum approach.

The second slender body validation case considered is that of Murman [20] who investigated a laminar hypersonic wake behind a 10 deg half-angle cone with a 1 in. base diameter at zero angle of attack in a helium wind tunnel. The helium freestream has a Mach number of 16.35, a pressure of 20.13 Pa, and a density of 2.922×10^{-3} kg/m^3. In our two-dimensional axisymmetric DSMC simulation, the computational domain extends 39×169 mm with 150×650 cells in the radial and flow directions, and each cell can be divided up to 20 subcells during the simulation. A time step of 5.0×10^{-8} s is used, and one simulated particle represents 5.0×10^{11} real particles in the DSMC simulation with radial weighting factors. There are a total of about 4 million simulated particles at the steady state, and the macroparameters are sampled from the 4000th to the 40,000th time step. Figure 5 presents the ratio of the wake flow axial *U* velocity (left) and density (right) to the freestream values along a radial direction at a location of 3 base diameters downstream of the cone base. It can be seen from Fig. 5 that there is less than 20% difference between the computational and experimental nondimensional axial velocity in the center flow, although the agreement improves significantly for larger radial values. Note that the experimental data [20] of the nondimensional velocity beyond 0.8 times of the base diameter is not available. The simulated nondimensional density curve also agrees well with the experimental data, which covers all of the important physical regions including the near-wake flow, expanding shock, leading shock, and freestream flows along the radial direction.

The third experimental case we consider is that of Dewey [21] who measured the laminar wake flow of a blunt cylinder with a diameter of 6.0 mm under zero angle of attack. The test gas was air, and the freestream has a Mach number of 6.0, a temperature of 49.77 K, and pressure of 217.04 Pa. We conducted a DSMC two-dimensional simulation to model this case as follows. The computational domain extends 12×24 mm with 200×400 cells in radial and flow directions, and each cell can be divided into up to 20 subcells during the simulation. A time step of 2.0×10^{-7} s is used, and one simulated particle represents 2.5×10^{13} real particles in the DSMC simulation with radial weighting factors. There are a total of about 4.2 million simulated particles at steady state, and the macroparameters are sampled from the 6000th to the 50,000th time step. Figure 6 compares the local total pressure in the cylinder wake region along the radial direction at a distance of 0.80 times the cylinder diameter from the cylinder centerline between the experimental data (symbols) and simulation result (line). It can be seen that again the DSMC result is in good agreement with the experimental data in the cylinder wake flow region.

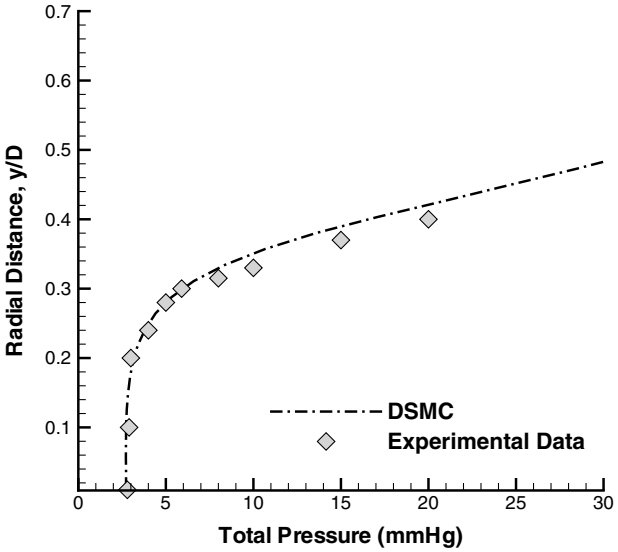

Fig. 6 Comparison of the total pressure along a radial direction at a distance of 0.80 times the cylinder diameter from the cylinder centerline between the experimental data (symbols) [21] and simulation results (lines).

To further verify our DSMC method of modeling blunt body wake flows, we test a blunt body case for the geometry shown in Fig. 2. The freestream flow is at an altitude of 85 km with a number density of 1.654×10^{20} molecules/m^3, a temperature of 180.65 K, and a velocity of 7000 m/s. The freestream is composed of two species, 23.72% O_2 and 76.28% N_2. The wall has a temperature of 1000 K with diffuse and full thermal accommodation boundary conditions. The set of chemical reactions for air species [8] that are included in the DSMC simulation are given in Table 1. (Note that E_a is the reaction activation enegery, and A and B are the constants in the Arrhenius reaction rate equation $k_f = AT^{-B} \exp -E_a/kT$.) In our two-dimensional axisymmetric DSMC simulation, the computational domain is 2×4 m with 200×400 cells in radial and flow directions, and each cell can be divided into up to 20 subcells during the simulation. A time step of 5.0×10^{-7} s is used, and one simulated particle represents 1.25×10^{13} real particles in the DSMC simulation with radial weighting factors. There are a total of about 4.5 million simulated particles at steady state, and the macroparameters are sampled from the 8000th to the 50,000th time step. Figure 7 compares the DSMC simulation results of Dogra et al. [3] and our calculations of the axial velocity (left) and nondimensional density (right) as the ratio of the local mass density to the freestream value along the radial direction at $b = 0.383$. In the current work, b refers to the axial distance from the base surface normalized to the base radius of 1.0 m. As shown in Fig. 7, the slope changes of axial velocity and density along the radial direction indicate the different flow regions, such as near-wake, expanding, bow shock, and freestream flows. Thus, the consistency of the simulation results along the radial direction between these two independent studies provide additional evidence as to the accuracy of the current numerical approach for modeling near-wake flows.

III. Results and Discussion

Near-wake flows are characterized by some important features, such as low density, high temperature, thermal nonequilibrium, chemical species separation, and recirculation. These features could potentially be sensitive to body geometry, that is, slender or blunt bodies due to the oblique or bow-shock characteristics, respectively. To quantitatively study near-wake flow, we investigate near-wake flowfields in this section at zero angle of attack behind a 10 deg half-angle cone (slender body) with a length of 1.0 m and a 70 deg blunt body as shown in Fig. 2, respectively.

The freestream conditions selected for the current slender and blunt body studies are similar and are given in Table 2. In the literature [23], various geometric lengths have been chosen as the characteristic length for nondimensionalization of parameters in reentry flows. For example, the nose radius is chosen for the forebody bow shock, and the body length is chosen for the flowfield of the whole vehicle. Because we are mainly interested in the near-wake region, the base radius will be chosen as the characteristic length in this work. Note that in the gas dynamics, a scale length based on the local density gradient was proposed by Bird [16] as the characteristic length to calculate local Knudsen number and estimate flow regimes. In the slender body wake region, it was found that the local characteristic length based on Bird's definition is about 0.1 m at (1.03, 0) and 0.27 m at (1.2, 0). Note that the slender body base is located at $x = 1.0$ m. Thus, the base radius, 0.1763 m, is on the same order as the local characteristic length in the wake region. The slender and blunt body wall temperatures are set to 1000 K, and a full thermal accommodation boundary condition is used in the DSMC calculations. The DSMC computational domain for the slender body is 0.5×2.0 m in the radial and axial directions with 100×400 cells, and for the blunt body is 4.0×8.0 m with 400×800 cells. Each cell can be divided into 20 subcells in the simulation so that the cell size is on the order of the local flow mean free path. A time step of 5.0×10^{-7} s is used, and the macroparameters are sampled from the 12,000th to the 60,000th time step in both cases.

Figures 8 and 9 show pressure (top), temperature (middle), and Mach number (bottom) contours for the slender and blunt body flows, respectively. As shown in Figs. 8 and 9, the near-wake flow is

Table 1 List of chemical reactions for air species

No.	Reaction	Enthalpy, $\times 10^{-19}$ J	A	B	E_a, $\times 10^{-19}$ J
1	$O_2 + N \rightarrow O + O + N$	8.197	5.593×10^{-12}	1.0	8.197
2	$O_2 + NO \rightarrow O + O + NO$	8.197	5.593×10^{-12}	1.0	8.197
3	$O_2 + N_2 \rightarrow N_2 + O + O$	8.197	1.198×10^{-11}	1.0	8.197
4	$O_2 + O_2 \rightarrow O_2 + O + O$	8.197	5.393×10^{-11}	1.0	8.197
5	$O_2 + O \rightarrow O + O + O$	8.197	1.498×10^{-10}	1.0	8.197
6	$N_2 + O \rightarrow O + N + N$	15.61	3.187×10^{-13}	0.5	15.61
7	$N_2 + O_2 \rightarrow O_2 + N + N$	15.61	3.187×10^{-13}	0.5	15.61
8	$N_2 + NO \rightarrow NO + N + N$	15.61	3.187×10^{-13}	0.5	15.61
9	$N_2 + N_2 \rightarrow N_2 + N + N$	15.61	7.968×10^{-13}	0.5	15.61
10	$N_2 + N \rightarrow N + N + N$	15.61	6.900×10^{-8}	1.5	15.61
11	$N_2 + NO \rightarrow N + O + N_2$	10.43	6.590×10^{-10}	1.5	10.43
12	$NO + O_2 \rightarrow N + O + O_2$	10.43	6.590×10^{-10}	1.5	10.43
13	$NO + NO \rightarrow N + O + O_2$	10.43	1.318×10^{-8}	1.5	10.43
14	$NO + O \rightarrow N + O + O$	10.43	1.318×10^{-8}	1.5	10.43
15	$NO + N \rightarrow N + O + N$	10.43	1.318×10^{-8}	1.5	10.43
16	$NO + O \rightarrow O_2 + N$	2.719	5.279×10^{-21}	−1	2.719
17	$N_2 + O \rightarrow NO + N$	5.175	1.120×10^{-16}	0	5.175
18	$O_2 + N \rightarrow NO + O$	−2.719	1.598×10^{-18}	−0.5	0.4968
19	$NO + N \rightarrow N_2 + O$	−5.175	2.490×10^{-17}	0	0

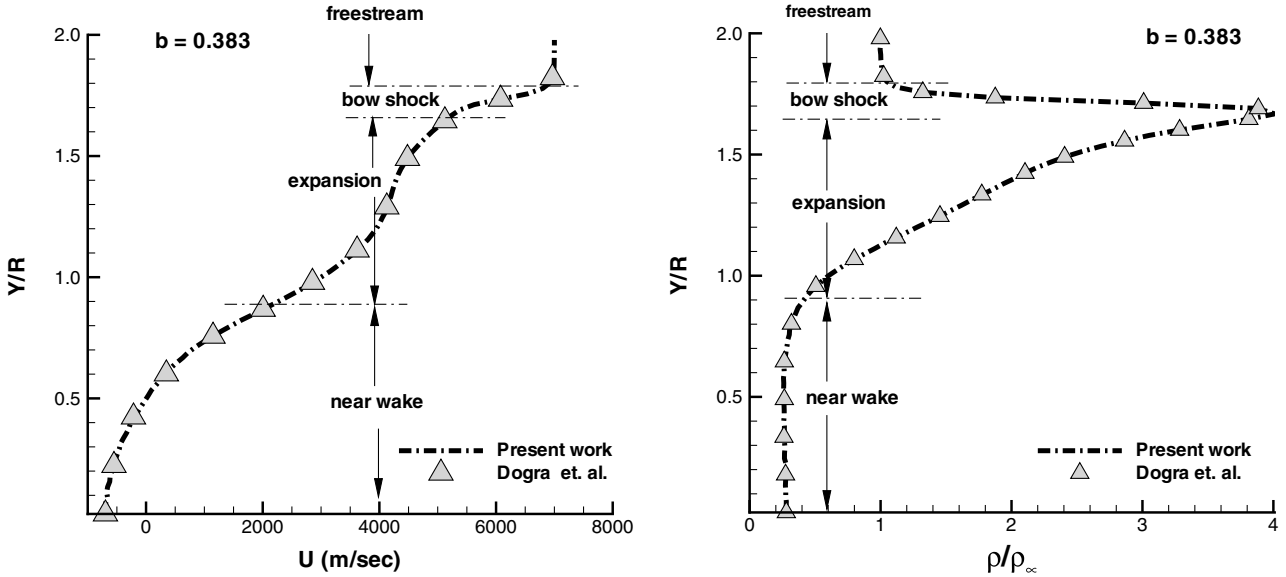

Fig. 7 Comparsion of axial velocity (left) and nondimensional density (0.383 m downstream of the base) for blunt body wake flow between the DSMC simulation results of Dogra et al. [3] and the calculations of this work.

characterized by features of low density, high temperature, and low velocity, and an oblique/bow shock separates the near-wake flow from the hypersonic freestream flow. Next, we analyze and compare the near-wake flows of a slender and blunt body.

A. Low Density in Near-Wake Flows

Figure 10 shows the normalized number density distributions along the radial direction at locations of $b = 0.57, 1.70, 3.40$ in the slender (top) and blunt (bottom) body wake regions. Note that b is the axial distance from the base surface normalized by the base radius. It can be seen that in the slender body wake center region, the gas number density is relatively constant, about 10 times less dense than the freestream number density. However, the gas number density in the blunt wake center region is about two times less dense at a b value of 0.57, and quite close to the freestream value at b values of 1.70 and 3.40. In both slender and blunt expanding regions, the gas number density decreases rapidly from shock toward the wake centerline. Note that the maximum number density along the radial direction coincides with the oblique and bow shocks for the slender and blunt body cases, respectively. As shown in Fig. 10, the gas in the oblique and bow shocks is several times denser than the freestream flow. Moving downstream (higher b values), the peak number density in the slender body oblique shock decreases rapidly, although this is not observed in the blunt bow-shock region. This is because the detached bow shock is much stronger than the attached oblique shock, thereby creating a longer near-wake flow which leads to a greater downstream distance required to observe a decrease in the shock number density.

Table 2 Freestream conditions for the slender and blunt body simulation

	Slender	Blunt
Height, km	80	85
Velocity, km/s	7.5	7.0
Mach no.	27.5	26.0
Temperature, K	185.0	180.65
Stagnation T, K	28139	24556
Pressure, Pa	1.068	0.4124
Stagnation P, Pa	4.63E + 7	1.21E + 7
Number density, mole/m^{-3}	4.18E + 20	1.65E + 20
Mean free path, m	3.0E − 3	7.3E − 3
N_2 mole fraction	79%	76.3%
O_2 mole fraction	21%	23.7%
Base radius, m	0.1763	1.0

Because of the difference of the oblique and bow-shock strength, the pressure in the near-wake region is different for the slender and blunt cases. Figure 11 shows the pressure normalized to the freestream value along the axial direction in the slender and blunt near-wake region. Although the gas number density in the near-wake region is lower than the freestream number density, the maximum near-wake pressures are approximately more than 5 and 20 times higher than the freestream pressure for the slender and blunt flows, respectively. This is because the temperature in the near-wake is much higher than the freestream temperature, as will be discussed in the next subsection. As the flow moves downstream, the near-wake pressure decreases due to expansion for both the slender and blunt cases. However, it takes a longer distance for the pressure to decrease in the blunt wake than in the slender wake, as shown in Fig. 11.

B. Temperature Jump and Velocity Slip in Near-Wake Flows

Figure 12 shows the flow axial velocity and temperature along the centerline in the near-wake region for the slender (top) and blunt (bottom) bodies. The maximum temperature at the centerline for the slender and blunt bodies is about 3400 and 4400 K, respectively, much higher than the freestream temperature of about 180 K. This is because most of the gas kinetic energy is converted to thermal energy in the slow-speed near-wake region, leading to a high gas temperature which impacts the thermal protection layer design of the base region. Note that the maximum temperature is approximately at the location of the rear stagnation region. Although the gas molecules in near-wake region may still have not enough energy to initiate chemical reactions, the gas temperature is sufficiently high to create significant amounts of the gas-surface ablation reactions [24]. Gas-surface reactions have not been modeled in this work, but will be studied in the future.

As shown in Fig. 12, there exists a temperature jump for both the slender and blunt body wake flows, with the flow temperature close to the base being about several hundred degrees higher than the base surface temperature of 1000 K. Moss et al. [25] studied temperature jump at the forebody stagnation point of a 5 deg half-angle cone vehicle at altitudes ranging from 70 to 110 km with a freestream velocity of 7.5 km/s. Comparing the magnitude of the temperature jump of Moss et al. [25] with this work, it can be seen that gas temperature jump at the forebody and afterbody stagnation points are approximately on the same order, about several hundred degrees. Thus, the phenomenon of temperature jump in the base region has the same importance as in the forebody region.

There are two stagnation locations along the wake flow centerline. The first one is close to the base wall, but due to the slow speed in the

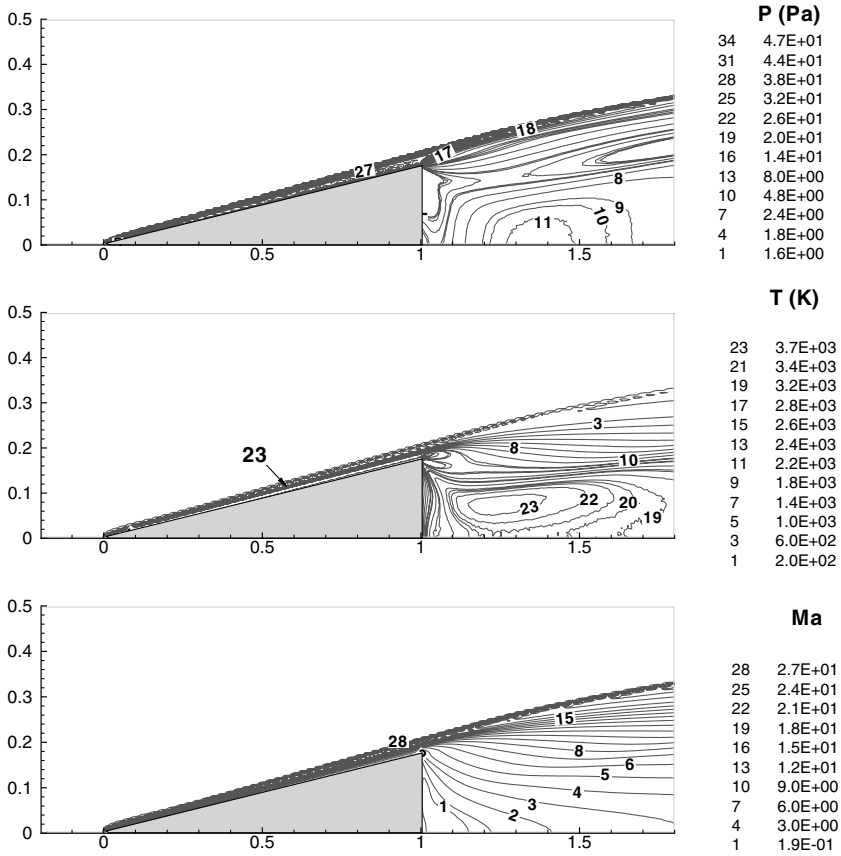

Fig. 8 Pressure (top), temperature (middle), and Mach number (bottom) contours for the slender body flow with a freestream velocity of 7500 m/s at 80 km. Axes are in meters.

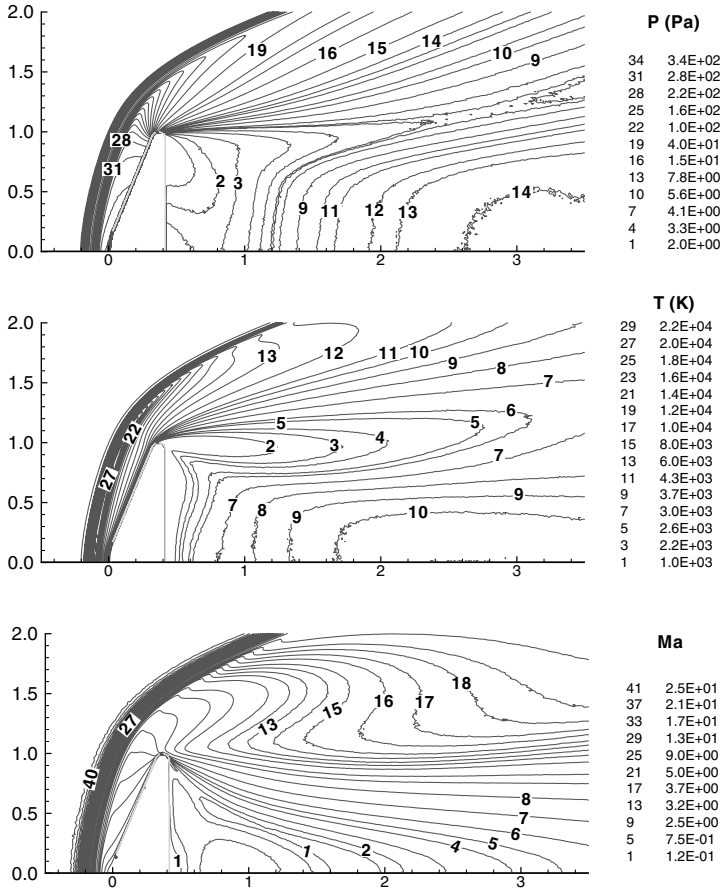

Fig. 9 Pressure (top), temperature (middle), and Mach number (bottom) contours for the blunt body flow with a freestream velocity of 7000 m/s at 85 km. Axes are in meters.

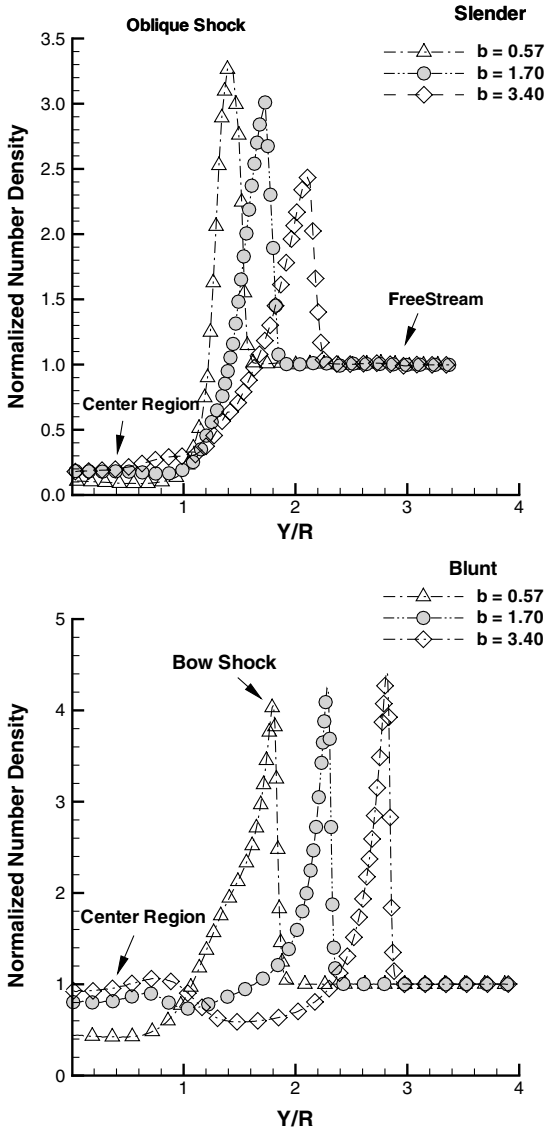

Fig. 10 Number density normalized to the freestream values along the radial direction in near-wake region for the slender (top) and blunt (bottom) bodies. The normalization factors for the slender and blunt body cases are 4.18E + 20 and 1.65E + 20 molecules/m^3, respectively.

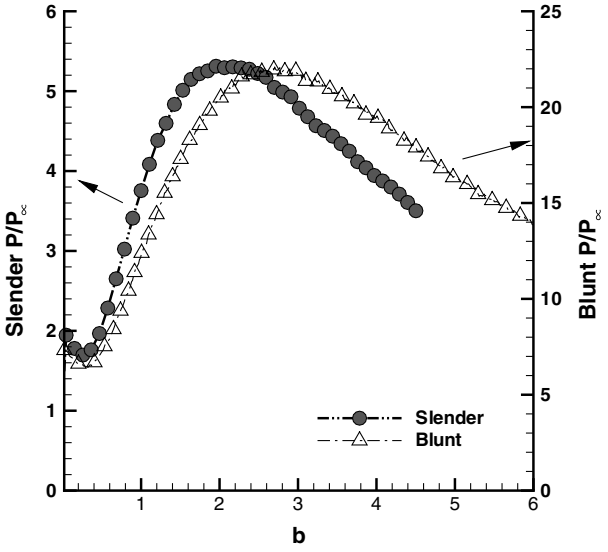

Fig. 11 The pressure distributions normalized to the freestream value along the centerline in the slender and blunt near-wake regions.

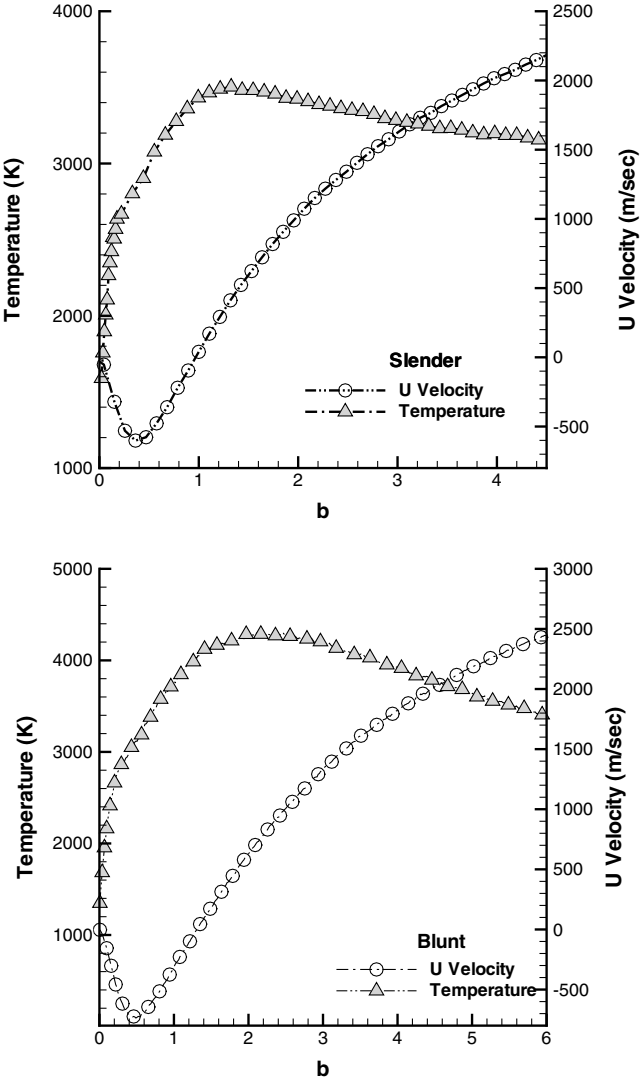

Fig. 12 Velocity and temperature along the centerline in near-wake region for the slender (top) and blunt (bottom) bodies.

near wake there is no velocity slip for either the slender or blunt bodies. The second stagnation point, known as the rear stagnation point, is located at a nondimensional position of about 0.92 and 1.24 for the slender and blunt flows, respectively. It can be seen from Fig. 12 that flow axial velocity at the location between these two stagnation points is negative, showing that there exists a recirculation region where the flow moves upstream. Thus, the normalized recirculation lengths, defined as the ratio of the recirculation length to the base radius, are 0.92 for the slender body and 1.24 for the blunt body. Note that for the blunt body case, Dogra et al. [3] predicted a nondimensional recirculation length of about 1.24 for the nonreacting flow, and 1.55 for the chemically reading flow. The difference in our recirculation value of 1.24 and that of Dogra et al. [3] of 1.55 is most likely due to our improved grid resolution. As will be discussed in Sec. III.E, the difference of the nondimensional recirculation length is caused by the shoulder gas expansion process, and the recirculation length in the near-wake flow is essentially proportional to the base radius for similar shoulder gas flow conditions.

C. Thermal Nonequilibrium in Near-Wake Flows

Hypersonic reentry flow is characterized by nonconstant specific heats, and molecular dissociation, and even ionization in some conditions. These phenomena, known as "real gas effects," makes it important to understand thermal nonequilibrium in terms of molecular translational, rotational, and vibrational temperatures.

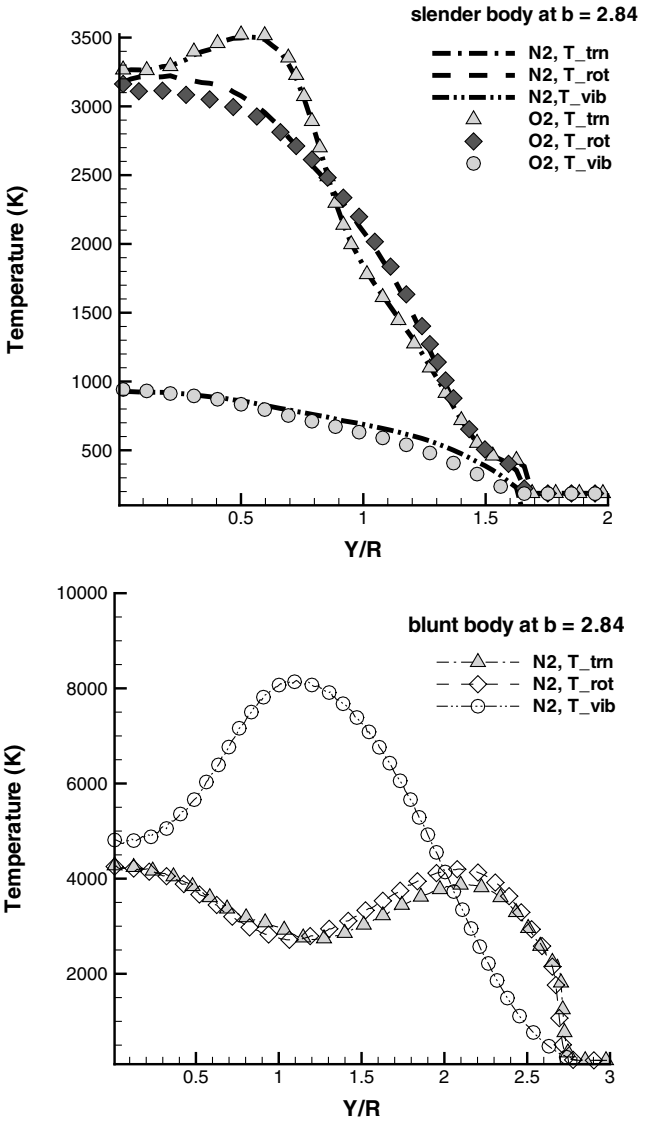

Fig. 13 Translation, rotational, and vibrational temperature distributions along the radial direction in the slender (top) and blunt (bottom) body wakes.

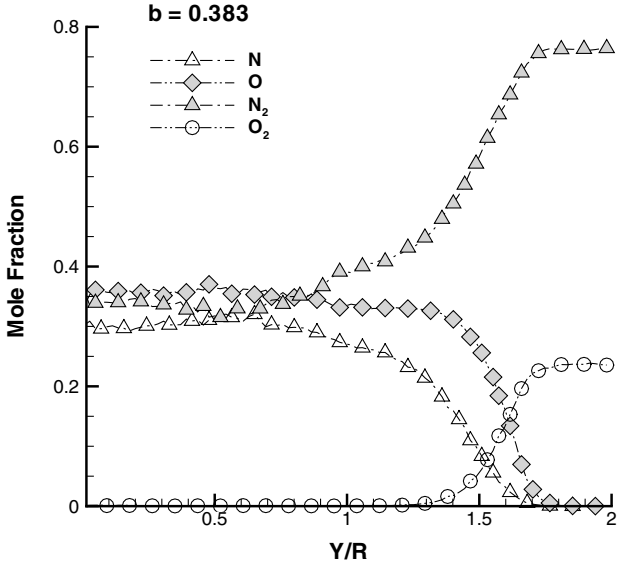

Fig. 14 Species mole fraction along the radial direction in the blunt body wake.

Figure 13 shows near-wake flow species translational, rotational, and vibrational temperatures along the radial direction for the slender (top) and blunt (bottom) bodies, respectively. It can be seen that, for both cases, the translational and rotational temperatures are almost equilibrated, whereas there exists significant nonequilibrium between both the translational and rotational temperatures with the vibrational temperature.

As shown in Fig. 13, the spatial profiles of the vibrational vs the translational and rotational temperatures are different in the wake region of the slender and blunt bodies. Moreover, the vibrational temperature in the wake of the slender body is generally lower than that of the blunt body, and is well below that of the translational and rotational temperatures. Compared with the slender body flow, the strength of the blunt body bow shock causes much more thermal excitation in the shock layer, leading to much higher vibrational temperatures. Because of the rarefied condition, there are not enough collisions to equilibrate the expanding gas as it expands from the shoulder to the near-wake base region. There are several reasons for the different thermal nonequilibrium phenomenon between vibrational mode and rotational and translational modes in the slender and blunt wake region. First, the species vibrational characteristic temperatures are so high that it is more likely that molecular inelastic collisions result in translation–rotation energy exchange rather than translation–vibrational energy exchange. Second, the blunt bow-shock spatial region of high molecular kinetic energy is larger than in the slender body case, facilitating the transfer of rotational and translational energy compared with the slender body case. Third, local gas temperature is sensitive to the gas number density and velocity, which further influences the rate of energy exchange among particles. The difference in the shock structure between slender and blunt body flows causes completely different nonequilibrium thermal spatial distributions.

Because of the relatively weak oblique shock, the degree of thermal nonequilibrium in the slender body flow decreases at locations away from the center flow. However, as the radial distance increases, the degree of thermal nonequilibrium in the blunt case first increases rapidly to a maximum value at about $1.15R$, then it decreases until the flow approaches the freestream. Note that the species O_2 temperatures are not shown in the blunt case because there are few O_2 molecules in the wake region due to the upstream shock dissociation process, as will be shown in Fig. 14. Figure 13 also shows that, at the axial location of $b = 2.84$, the freestream condition is reached at about $1.7R$ and $2.8R$ for the slender and blunt body cases, respectively. As expected, the blunt body has a wider wake flow due to a larger bow-shock region.

D. Special Separation in Near-Wake Flows

It is important to accurately understand species distribution in the near-wake region because it may contribute to the erosion of base surface thermal protection materials as discussed in the literature [26]. Because of the weakness of the attached oblique shock, there are almost no gas chemical reactions in the slender body flows. However, the detached bow shock for the blunt body is so strong that the gas temperature may be more than 22,000 K, as was shown in Fig. 9. The high gas temperature leads to a significant number of chemical reactions in the blunt body shock layer flow, which initiates chemical species separation in the blunt body near-wake region.

Figure 14 shows the near-wake blunt body flow species mole fractions along the radial direction at $b = 0.383$. Because of the dissociation processes of the N_2 and O_2 molecules in the high-temperature bow-shock region, there exists large amounts of N and O molecules in the blunt body flow. Note that the N and O molecules could potentially recombine to form NO molecules. However, it was observed that the recombined NO molecules usually dissociate back to N and O molecules due to the high gas temperature, and the mole fraction of NO molecules is less than 1% in the computational domain. It can be seen from Fig. 14 that, in the wake region, there are almost no oxygen molecules, and the relative mole fraction of wake species is about 30% of N, 36% of O, and 34% of N_2 molecules, similar to the simulation results of Dogra et al. [3]. At outer radial distances, the N and O mole fractions decrease, whereas the N_2 and

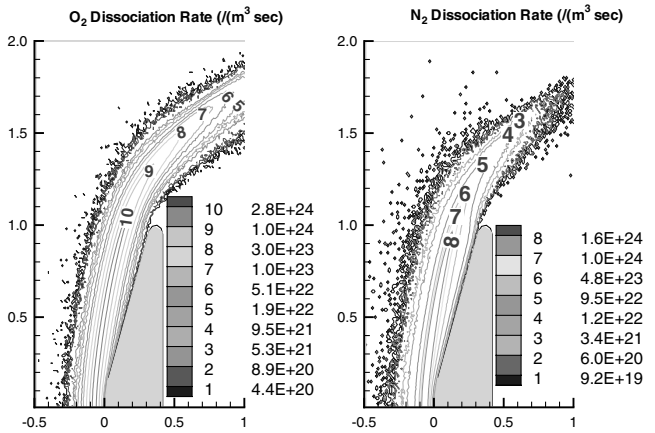

Fig. 15 Distribution of O_2 and N_2 dissociation rates ($m^{-3}\,s^{-1}$) in the blunt body flow.

O_2 mole fractions increase to the freestream values. For these reasons, species separation exists in the blunt body wake flow.

There are two reasons that may contribute to species separation. First, the spatial N_2 and O_2 dissociation rates are sensitive to variations in the gas temperature, relative velocity, and number density. Second, the lighter N and O atoms have different diffusion speeds from the heavier N_2 and O_2 molecules. Figure 15 shows the distribution of O_2 and N_2 dissociation rates in the blunt body flow. The dissociation rate Rd is calculated from the number of dissociation cases N sampled from the DSMC simulation in each cell as

$$Rd = \frac{NF_nW_r}{\Delta V \Delta T} \tag{1}$$

where F_n refers to the number of real molecules represented by one simulated molecule, W_r is the radial weighting factor, ΔV is the cell volume, and ΔT is the sample time. It can be seen that most of the O_2 and N_2 dissociation occurs in the bow-shock region, where N an O atoms are initially generated and then diffuse to the near-wake region. The different diffusion speeds for the lighter atoms and heavier molecules cause species separation in the blunt body near-wake region. Note that the dissociation of O_2 and N_2 molecules is not observed in the blunt body wake region. Although the freestream N_2 number density is more than three timer larger than the O_2 number density, the O_2 dissociation rate is slightly higher than the N_2 dissociation rate because the O_2 molecule has a lower dissociation activation energy than the N_2 molecule. The species separation does not exist in the slender body flow because there is almost no molecular dissociation process due to relatively low temperatures in the attached oblique shock.

E. Near-Wake Vortex Structure

One important feature in the near-wake flow is the recirculation region, which is separated from the outer hypersonic flow by a dividing streamline, item (d) in Fig. 1. As discussed by Lamb and Oberkampf [22], the dividing streamline is located in a region known as the free shear layer, shown here in Fig. 16. The figure shows an example of our computed flow velocities parallel to the dividing streamline along from the indicated profile through the shear layer region. The computed free shear layer velocity profile of Fig. 16 is consistent with the base flow features, discussed in Fig. 4 by Lamb and Oberkampf [22]. The shear stress, proportional to the velocity derivative, changes the gas direction at the dividing streamline in the center of the free shear layer, as can be observed in Fig. 16. The formation mechanism of a vortex is determined by the separation of shoulder expanding waves from the base surface. Because the flow features in the recirculation region, such as low velocity, high temperature, and low density, are different from other regions, it is important to characterize the recirculation size in the near-wake flow to predict the wake flow impact on vehicle stability, gas-surface

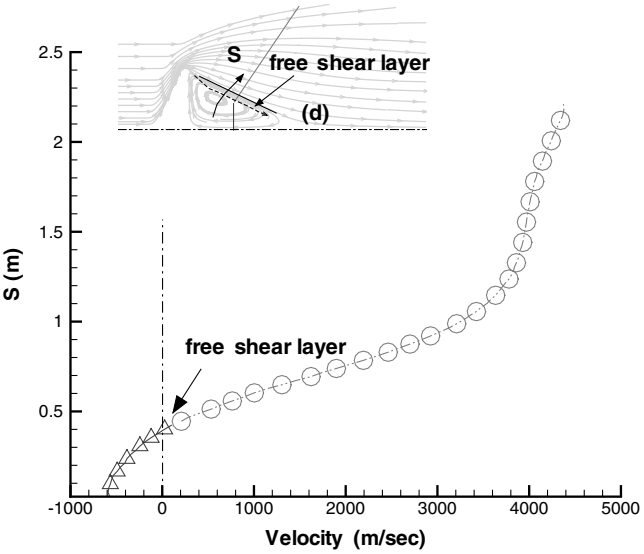

Fig. 16 Velocity parallel to the dividing streamline in the free shear layer of the near-wake flow. S is the distance along a line perpendicular to the dividing streamline.

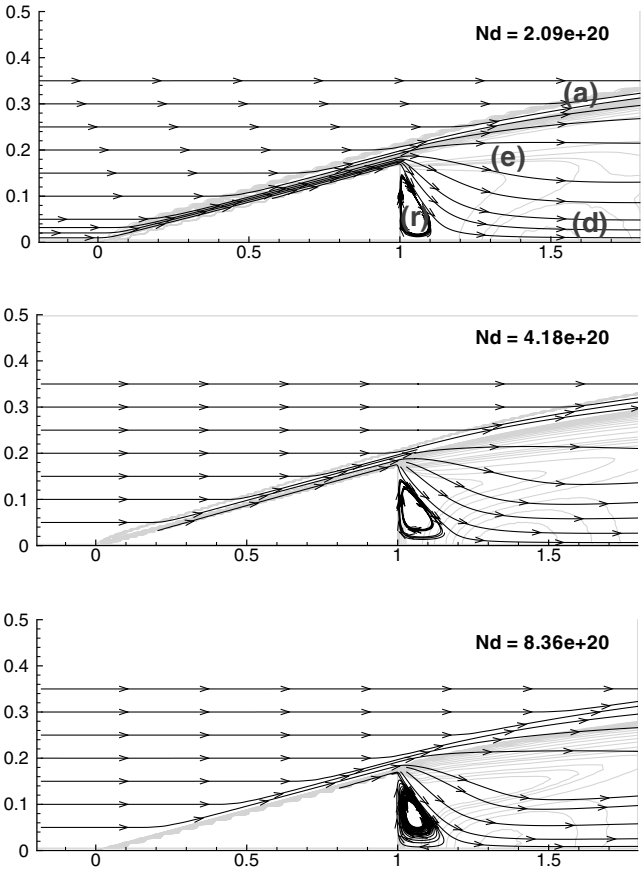

Fig. 17 Streamlines for the slender body flows with various freestream flow number densities. Axes are in meters. The symbols identify various near-wake flow regions, as shown in Fig. 1.

chemical reactions, and near-wake radiation. The dividing streamline (d) and the recirculation region, as discussed in Fig. 1, will be clearly presented in the streamline plots of Figs. 17 and 18 for the slender and blunt near-wake flows in this subsection.

First, we investigate the impact of the freestream number density on the vortex structure in the near-wake region. Figures 17 and 18 show streamlines for the slender and blunt bodies for various

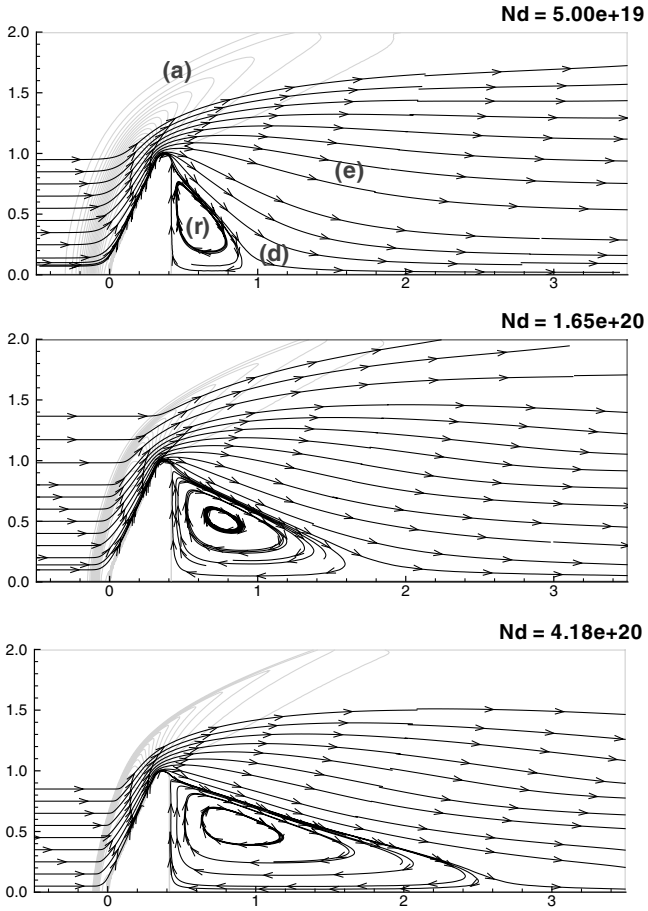

Fig. 18 Streamlines for the blunt body flows with various freestream number densities N_d. Axes are in meters. The symbols identify various near-wake flow regions, as shown in Fig. 1.

freestream number density cases. The DSMC simulation results suggest that the gas number density at the shoulder increases as the freestream number density increases for both the slender and blunt body cases, which further impacts the gas expansion and near-wake flow. As can be seen from Fig. 17, the recirculation length for the slender body does not change significantly as the freestream number density increases. However, the recirculation length in the blunt body wake region increases significantly, from 0.47 to 1.24 and 2.08 m, as the freestream number density increases from 5.00×10^{19} to 1.65×10^{20} and 4.18×10^{20} molecules/m^3. Although the freestream number density has almost the same impact on the gas state at the shoulder for the slender and blunt bodies, it has less impact on the recirculation length for the slender body, due to the smaller space available for flow expansion compared with the blunt body.

Figure 19 shows the Reynolds number distributions along the near-wake flow centerline for the slender (left) and blunt (right) cases. The Reynolds number can be related to the Mach number M and the mean free path λ as [27],

$$Re = \frac{LM}{\lambda}\sqrt{\frac{\pi\gamma}{2}} \tag{2}$$

where γ is the ratio of specific heats. For the different freestream densities, it can be seen that the Reynolds numbers in the recirculation region for these cases are small, less than 100. The feature of low Reynolds number in the near-wake flow has been widely discussed in the literature [28,29]. As the Reynolds number increases, the recirculation length is similar for the slender body cases, whereas it is quite different for the blunt body cases. It has been shown in Figs. 17 and 18 that the recirculation length is larger in the blunt cases than the slender cases regardless of the Reynolds number. Thus, near-wake Reynolds number may not be related to the recirculation length in the rarefied wake region. Assuming an ideal gas and chemical frozen model, Grasso and Pettinelli [1] investigated the recirculation structure in laminar near-wake hypersonic flows by solving the laminar Navier–Stokes equations. They also found that the Reynolds number cannot be used for characterizing the near-wake structure and that the base flowfields mainly depend on the upstream shoulder gas expansion.

To further examine the impact of freestream Mach and Reynolds numbers on the vortex structure in the near-wake flow region, we decreased the freestream velocity to 4500 and 2000 m/s, causing a decrease of Mach number to about 16.7 and 7.4. It was observed for both slender and blunt bodies that there is no observable changes of the near-wake recirculation length as the freestream velocity decreases. This phenomenon can be explained by the well-known "hypersonic freeze" or "Mach number independence principle" [23], which means that further increase in Mach number produces no qualitative change in the near-wake region. This is again because the near-wake property is determined by the shoulder gas expanding process, and the hypersonic freestream velocity has little impact on the shoulder gas, which is mainly controlled by the development of surface boundary layer. Thus, we may conclude that the freestream velocity has little impact on the near-wake flow for both the slender and blunt bodies.

On the other hand, because the base radius determines the space available for the shoulder gas expansion, we may expect that it is a key geometric parameter that impacts the recirculation length in the near-wake flow. A summary of three group studies [30], presented in Table 3, shows that the recirculation length in the slender body near-wake flow increases as the base radius increases. First, as the cone half-angle increases from 10 to 20 and 30 deg, whereas the cone length remains 1.0 m, the base radius correspondingly increases from 0.1763 to 0.3640 and 0.5774 m. It was verified that the recirculation length in the near-wake region increases significantly from 0.16 m for the 10 deg cone angle to 0.26 and 0.58 m for the 20 and 30 deg cones, respectively. Second, as the cone nose radius increases from

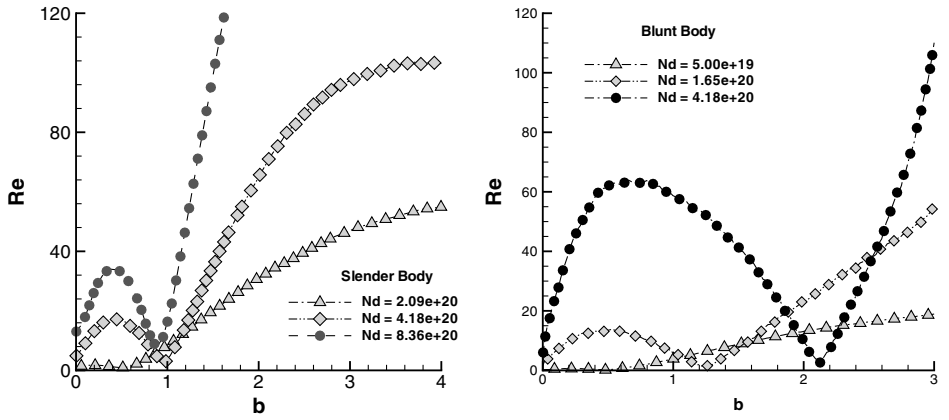

Fig. 19 Reynolds number along the wake flow centerline for the slender (left) and blunt (right) body flows at various freestream number densities.

Table 3 The recirculation length in the near-wake flow as a function of the base radius.[a]

	Cone geometry				
Case	Nose radius, m	Half-angle, deg	Length, m	Base radius, m	Recirculation length, m
Group 1	0.0	10	1.0	0.1763	0.16
	0.0	20	1.0	0.3640	0.26
	0.0	30	1.0	0.5774	0.58
Group 2	0.0	10	1.0	0.1763	0.16
	0.1	10	1.0	0.2717	0.30
	0.2	10	1.0	0.3672	0.45
Group 3	0.0	10	2.0	0.3526	0.40
	0.0	10	2.5	0.4408	0.52
	0.0	10	3.0	0.5290	0.68

[a]Full DSMC simulation results are presented in [30].

0.0 to 0.1 and 0.2 m, with a half-angle of 10 deg and a length of 1.0 m, the base radius increases from 0.1763 to 0.2717 and 0.3672 m, respectively. In [30], it was shown that as the base radius increases, the recirculation length in the near-wake increases significantly from 0.16 to 0.30 and 0.45 m. Finally, we compare the near-wake vortex from the flows around the 10 deg half-angle slender bodies with a cone length of 2.0, 2.5, and 3.0 m, corresponding to a base radius of 0.3526, 0.4408, and 0.5290 m, respectively. As the base radius increases, the recirculation length in the near-wake increases significantly from 0.40 to 0.52 and 0.68 m [30].

The normalized results for the first and second group cases are not discussed here because the changes in cone angles and nose radius greatly impact the shock formation, surface boundary development, and boundary-layer separation such that the normalized results can not clearly show the relationship of the recirculation flow to the base radius. Figure 20 shows the normalized recirculation structure for the third group. A single figure is shown because, when the axes are normalized to the base radius, the base recirculation sizes are almost identical for the three cases discussed in the third group. This may also be seen by dividing the recirculation length values given in Table 3 by the respective base radius. To quantitatively show these results, the axial velocity and number density for various cone lengths are shown in Fig. 21 along the centerline, normalized to the base radius. As shown in the left figure of Fig. 21, the three cases in the last group have the same normalized axial velocity curves, as well as the normalized stagnation locations. Because the recirculation region is characterized by negative velocities, the normalized recirculation lengths are almost the same for these three cases. Thus, it can be concluded that the recirculation length in near-wake flow is proportional to the base radius because it determines the available space for the shoulder gas expansion process.

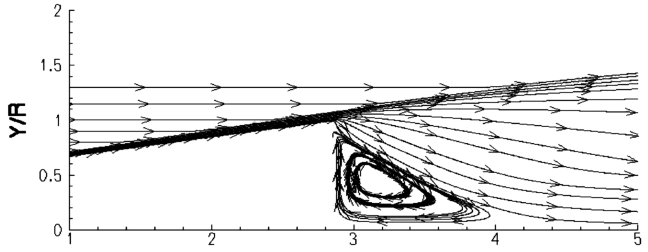

Fig. 20 Streamlines for flows around 10 half-degree slender bodies of 2.0, 2.5, and 3.0 m in length with a freestream velocity of 7500 m/s at 80 km. Axes are normalized to the base radius values of 0.3256, 0.4408, and 0.5290 m.

IV. Conclusions

The direct simulation Monte Carlo method has been applied in this work to study the near-wake slender and blunt body flows. The purpose of this work is to compare and contrast rarefied slender and blunt body wake flow features for the hypersonic reentry condition. To demonstrate the accuracy of the DSMC approach, three experimental cases and one independent computational case have been used to validate our DSMC calculations for the near-wake slender and blunt body flows.

It has been shown that the near-wake flow density is about 10 and 2 times less dense than the freestream density for the slender and blunt bodies, respectively. Because the bow shock is much stronger than the oblique shock, the decrease of number density and pressure in the blunt wake region is less than in the slender wake region. It was found that temperature jump exists in both slender and blunt wake flows investigated in this work, however, there is no velocity slip for either

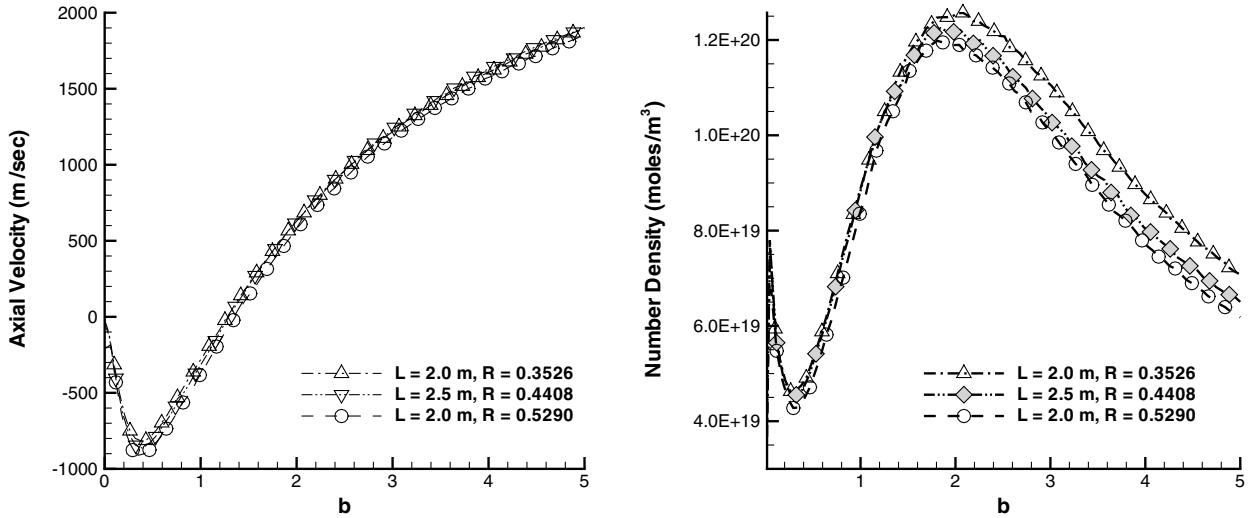

Fig. 21 Velocity and number density along the near-wake centerline normalized to the cone radius for flows around 10 half-degree slender bodies of 2.0, 2.5, and 3.0 m length with a freestream velocity of 7500 m/s at 80 km.

slender or blunt bodies due to the slow speed in the near-wake region. It has been shown that for both slender and blunt flows studied in this work, the translational and rotational wake temperatures are almost equilibrated, whereas the extent of nonequilibrium between these two temperatures with the vibrational temperature is different. Because of variations of the spatial dissociation rates and molecular diffusion rate, chemical species separation is observed in the blunt body wake flow. Because of the weakness of the attached oblique shock, there is almost no gas chemical reaction in the slender body flow.

Similar to earlier work, the DSMC computations show that the hypersonic freestream Mach number has little impact on the near-wake flow for the slender and blunt bodies, a phenomena known as "hypersonic freeze." However, the freestream number density has more impact on the recirculation length for the blunt body due to larger space available for flow expansion. It was also found that the recirculation length is not influenced by the Reynolds number for the laminar wake flows presented in this work, but rather is proportional to the base radius, found to be the characteristic length in the rarefied near-wake region flow.

Acknowledgments

The research performed at the Pennsylvania State University was supported by the NASA Ames Research Center through the Eloret Agreement No. 85224 entitled "Stardust Post-Flight Data Analysis" and the Air Force Office of Scientific Research Grant No. F49620-02-1-0104 whose support is gratefully acknowledged. Special thanks are to M. Ivanov of the Institute of Theoretical and Applied Mechanics, Russia for the use of the original SMILE code.

References

[1] Grasso, F., and Pettinelli, C., "Analysis of Laminar Near-Wake Hypersonic Flows," *Journal of Spacecraft and Rockets*, Vol. 32, No. 6, Dec. 1995, pp. 970–980.

[2] Grasso, F., and Pettinelli, C., "Nonequilibrium Effects in Near-Wake Ionizing Flows," *AIAA Journal*, Vol. 35, No. 7, July 1997, pp. 1151–1163.

[3] Dogra, V. K., Moss, J. N., Wilmoth, R. G., Taylor, J. C., and Hassan, H. A., "Effects on Chemistry on Blunt-Body Wake Structure," *AIAA Journal*, Vol. 33, No. 3, March 1995, pp. 463–469.

[4] Lin, T. C., Sproul, L. K., Kim, M., Olmos, M., and Feiz, H., "Hypersonic Reentry Vehicle Wake Flow Fields at Angle of Attack," AIAA Paper 2006-582, Jan. 2006.

[5] Johnson, J. E., Starkey, R. P., and Lewis, M. J., "Aerodynamic Stability of Reentry Heat Shield Shapes for a Crew Exploration Vehicle," *Journal of Spacecraft and Rockets*, Vol. 43, No. 4, 2006, pp. 721–730.

[6] Gnoffo, P. A., "Planetary-Entry Gas Dynamics," *Annual Review of Fluid Mechanics*, Vol. 31, Jan. 1999, pp. 459–494. doi:10.1146/annurev.fluid.31.1.459

[7] Taylor, R. L., Melcher, B. W., II, and Washburn, W. K., "Studies of the Luminous Hypersonic Wake," *AIAA Journal*, Vol. 2, No. 10, Oct. 1964, pp. 1731–1738.

[8] Gimelshein, S. F., Levin, D. A., and Collins, R. J., "Modeling of Glow Radiation in the Rarefied Flow About an Orbiting Spacecraft," *Journal of Thermophysics and Heat Transfer*, Vol. 14, No. 4, Dec. 2000, pp. 471–479.

[9] Moss, J. N., Mitcheltree, R. A., Dogra, V. D., and Wilmoth, R. G., "Direct Simulation Monte Carlo and Navier–Stokes Simulations of Blunt Body Wake Flows," *AIAA Journal*, Vol. 32, No. 7, July 1994, pp. 1399–1406.

[10] Gosse, R., and Candler, G., "Ablation Modeling of Electro-Magnetic launched Projectile for Access to Space," AIAA Paper 2007-1210, Jan. 2007.

[11] Palaninathan, R., and Bindu, S., "Modeling of Mechanical Ablation in Thermal Protection System," *Journal of Spacecraft and Rockets*, Vol. 42, No. 6, 2005, pp. 971–979.

[12] Anon., "America at the Threshold," Reports on the Synthesis Group on America's Space Exploration Initiative, Superintendent of Documents, U.S. Government Printing Office, Washington, D.C., 1991, p. 59.

[13] Wright, M. J., Milos, F. S., and Tram, P., "Afterbody Aeorheating Flight Data for Planetary Probe Thermal Protection System Design," *Journal of Spacecraft and Rockets*, Vol. 43, No. 5, Sept.–Oct. 2006, pp. 929–943.

[14] Berger, S. A., *Laminar Wakes*, Elsevier, New York, 1971, p. 294.

[15] Martin, J. J., *Atmospheric Reentry: An Introduction to Its Science and Engineering*, Prentice–Hall, New York, 1966, p. 264.

[16] Bird, G. A., *Molecular Gas Dynamics and the Direct Simulation of Gas Flows*, Oxford Science Publ., New York, 1994, p. 458.

[17] Ivanov, M. S., Markelov, G. N., and Gimelshein, S. F., "Statistical Simulation of Reactive Rarefied Flows: Numerical Approach and Application," AIAA Paper 98-2669, June 1998.

[18] Holden, M. S., "Experimental Studies of the Effect of Mass Addition on the Low-Altitude Turbulent Wake Behind Sharp Slender Cones," *Fluid Dynamics, Plasma Dynamics and Lasers Conference, 22nd*, AIAA Paper 1991-1774, June 1991.

[19] Todisco, A., and Pallone, A. J., "Near Wake Flow Field Measurements," *AIAA Journal*, Vol. 3, No. 11, 1965, pp. 2075–2080.

[20] Murman, E. M., "Experimental Studies of a Laminar Hypersonic Cone Wake," *AIAA Journal*, Vol. 7, No. 9, 1969, pp. 1724–1730.

[21] Dewey, C. F., "Near Wake of a Blunt Body at Hypersonic Speeds," *AIAA Journal*, Vol. 3, No. 6, 1965, pp. 1001–1010.

[22] Lamb, J. P., and Oberkampf, W. L., "Review and Development of Base Pressure and Base Heating Correlation in Supersonic Flow," *Journal of Spacecraft and Rockets*, Vol. 32, No. 1, 1995, pp. 8–23.

[23] Anderson, J. D., Jr., *Hypersonic and High-Temperature Gas Dynamics*, AIAA, Reston, VA, 2000.

[24] Suzuki, T., Furudate, M., and Sawada, K., "Unified Calculation of Hypersonic Flowfield for a Reentry Vehicle," *Journal of Thermophysics and Heat Transfer*, Vol. 16, No. 1, 2002, pp. 94–100.

[25] Moss, J. N., Cuda, V., and Simmonds, A. L., "Nonequilibrium Effects for Hypersonic Transitional Flows," AIAA Paper 1987-0404, Jan. 1987.

[26] Zhong, J., Titov, E., Levin, D. A., Picetti, D. J., and Akasmentov, D., "Numerical Simulation of a Microflow in an Expanding Channel," AIAA Paper 2006-3597, 2006.

[27] Schaaf, S. A., and Chambre, P. L., *Flow of Rarefied Gases*, Princeton Univ. Press, Princeton, NJ, 1961.

[28] Berger, S. A., and Viviand, H., "Effect of Base Bleeding on the Near Wake for Very Low Reynolds Numbers," *AIAA Journal*, Vol. 3, No. 11, 1965, pp. 2154–2157.

[29] Reeves, B. L., and Lees, L., "Theory of Laminar Near Wake of Blunt Bodies in Hypersonic Flow," *AIAA Journal*, Vol. 3, No. 11, 1965, pp. 2061–2074.

[30] Zhong, J., Ozawa, T., and Levin, D. A., "Modeling of Hypersonic Wake Flows of Slender and Blunt Bodies," AIAA Paper 2007-0612, Jan. 2007.

C. Kaplan
Associate Editor